IJESRT: 8(6), June, 2019 ISSN: 2277-9655

International Journal of Engineering Sciences &Research Technology

(A Peer Reviewed Online Journal)
Impact Factor: 5.164

IJESRT

Chief Editor
Dr. J.B. Helonde

Executive Editor
Mr. Somil Mayur Shah

Website: www.ijesrt.com Mail: editor@ijesrt.com

IJESRT
INTERNATIONAL JOURNAL OF ENGINEERING SCIENCES & RESEARCH TECHNOLOGY

CFD ANALYSIS OF TURBULENT SWIRLING FLOW CHARACTERISTICS IN A RANQUE-HILSCH VORTEX TUBE USING A RANS BASED TURBULENCE MODEL

C. B. Karthik Vigneshwar[*1] **&Peter J. Disimile**[2]
[*1]MS Aerospace Engineering, University of Cincinnati, Cincinnati, OH, US
[2]Associate Professor, Department of Aerospace Engineering, University of Cincinnati, Cincinnati, OH, US

DOI: 10.5281/zenodo.3240276

ABSTRACT

The present paper is focused on the computational analysis of the flow field inside a vortex tube using RANS based two-equation turbulence model $Std\ k-\epsilon$. The flow inside the vortex tube is a highly swirling one with very high values of swirl number. The current 3D CFD model was validated using published experimental data and was found to have a very good agreement in terms of total temperature predictions at the hot and cold outlets. The flow field was then compared to another published research study which utilized a higher order model, LES and was found to have qualitative differences between the tangential velocity profiles and the distributions of the free and forced vortex regions. The axial velocities and static temperature profiles on the other hand had a better agreement. With an idea of the strength and the weakness of the $Std\ k-\epsilon$ model, further analysis was done with respect to the flow properties i.e. Vorticity, Strain Rate and Reynolds Stress to provide a well-documented flow field of the flow inside vortex tube and explanations to the different phenomena observed are also presented.

KEYWORKS: Vortex Tube; Reynolds Averaged Navier Stokes (RANS); Computational Fluid Dynamics (CFD); energy separation; swirl flow; turbulence; vorticity; strain rate; Reynolds stress.

1. INTRODUCTION

A vortex tube is a passive device in which a pressurized gas enters through an inlet, swirls and is separated into two distinct flows, a hot (annular flow) and cold (core flow) which move in a helical trajectory through the device. When these flows move in the same direction, the vortex tube is called as a parallel flow vortex tube and when they move in the counter directions, it referred to as a counter-flow vortex tube. The process by which this energy separation occurs is surrounded by much controversy. In an attempt to improve the performance and understand the energy separation process, numerous studies on the flow field inside the vortex tube have been performed.

2. PREVIOUS WORKS ON VORTEX TUBE

One of the earliest experimental investigations on a vortex tube was done by J.P. Harnett & E.R.G Eckert [1]. Here, the authors measured the component velocities (u, v & w), total temperatures and pressures at various axial locations inside a relatively large vortex tube. Analytical comparisons were done between swirl flows in vortex tube and other types of flows such as Couette flow and Poiseuille flow (with and without rotation) to highlight the parameters important for energy separation. Brunn [2] also performed an experimental investigation, but with higher fidelity instrumentation and acquired data at more axial locations within the vortex tube. As a result of his analysis, he also put forth a possible cause of energy separation. Chang et al. [3] performed experimental studies on tangentially injected turbulent swirling flows and also provided some very good insight regarding the characteristics of such flows.

Extensive computational vortex tube studies have been performed by many researchers. Fröhlingsdorf & Unger [4] performed a comparison against experimental results using a 2D axisymmetric CFD model of the vortex tube. They found that when using the $Std\ k-\epsilon$ model, the model over predicted the tangential velocity profiles which deviated from the measured experimental values. They then implemented a correction factor from Keyes [5] to calculate the turbulent viscosity and the new model constants produced results which were in good agreement with the experiments. T. Dutta et al. [6] compared different turbulent models and found the $Std\ k - \epsilon$ to work better in terms of temperature predictions as the results were close to experimental values. Dutta et al., also applied the $SST\ k - \omega$ and $Std\ k - \omega$ models and found them to be slightly less accurate than the initial $Std\ k - \epsilon$ in terms of temperature predictions. Likewise, their results using the $RNG\ k - \epsilon$ model was found to deviate significantly in terms of temperature predictions from those obtained from the experiments. Secchiaroli et al. [7] performed numerical simulation on the vortex tube and computed the flow field using LES, RSM and RNG $k - \epsilon$ models. They found the LES (Large Eddy Simulation) and RSM (Reynolds Stress Model) to agree with each other in terms of velocity predictions and the RNG $k - \epsilon$ (Renormalization Group) to agree well near the inlet, however deviate at downstream axial locations.

Most other computational studies are focused on geometrical modifications to the vortex tube and studying its effect on the temperature separation phenomenon. Rajagopalan & Disimile [8] performed an extensive computational study on the effect of geometrical modifications such as L/D ratio, number of inlets, ratio of the diameter of swirl chamber, hot exit cone valve to the diameter of the vortex tube and cold orifice diameter on the performance of the vortex tube. Thakare et al. [9] performed both experimental and CFD studies on vortex tube by varying the cold fraction (ε), number of inlets, diameter of inlet nozzles, L/D ratio, straight & helical inlet nozzles, etc. and computed the performance of the vortex tube. They also compared the different turbulent models and concluded that the RSM worked best in terms of overall agreement with the experimental results. Bramo and Pourmahmoud [10] performed a detailed computational study changing the L/D ratio of the vortex tube. They also studied the effect of the L/D ratio on the location of the stagnation point. Stagnation point is the location where the axial velocity at the centerline of the vortex tube goes to zero and changes sign in further downstream axial locations. This is the location where the maximum total temperature has been observed in the annular flow. The authors found that the geometry in which the stagnation point was the nearest to the hot exit produced the highest total temperature difference in their computations.

From the literature survey it was observed that the turbulence model was the most important component of the analysis as the velocity profiles and ultimately the temperature and turbulence profiles depend on the model being used. The energy separation phenomenon is dependent on the turbulence properties of the flow within the vortex tube and the calculation of these quantities is also strongly dependent on the turbulence model being utilized. Of the available RANS (Reynolds Averaged Navier Stokes) models, RSM was found to provide the best agreement with experiment for the vortex tube study since it was able to predict the temperatures and the flow profiles inside the vortex tube with good accuracy. The two equation models like the $Std\ k - \epsilon$, $Std\ k - \omega$ & $SST\ k - \omega$ predicted temperatures with good accuracy, however, were poorer in agreement when predicting flow properties.

In the current study, the $Std\ k - \epsilon$ model was applied since it is the most widely used model in the vortex tube studies and also well documented one, to study the turbulent flow field inside the vortex tube and go on to provide a plausible explanation for the energy separation effect in light of the analyzed flow field.

3. COMPUTATIONAL MODEL

Geometry

To obtain a reliable model for in the current study, a validated model was developed based on the work of Skye et al. [11]. A 3D isometric view of the Vortex tube geometry used in the present study is presented in Figure 1. The Skye et al. [11] model was selected because they had provided experimental data for various cold mass fractions (ε), had a detailed description of the vortex tube geometric parameters from which the model could be accurately recreated, and they complimented their experimental results with a 2D axisymmetric computational model. Therein lies the major difference in the current simulation which utilized a 3D model of the vortex tube. The physical dimensions used for the vortex tube model are presented in table below with reference made to Figure 1.

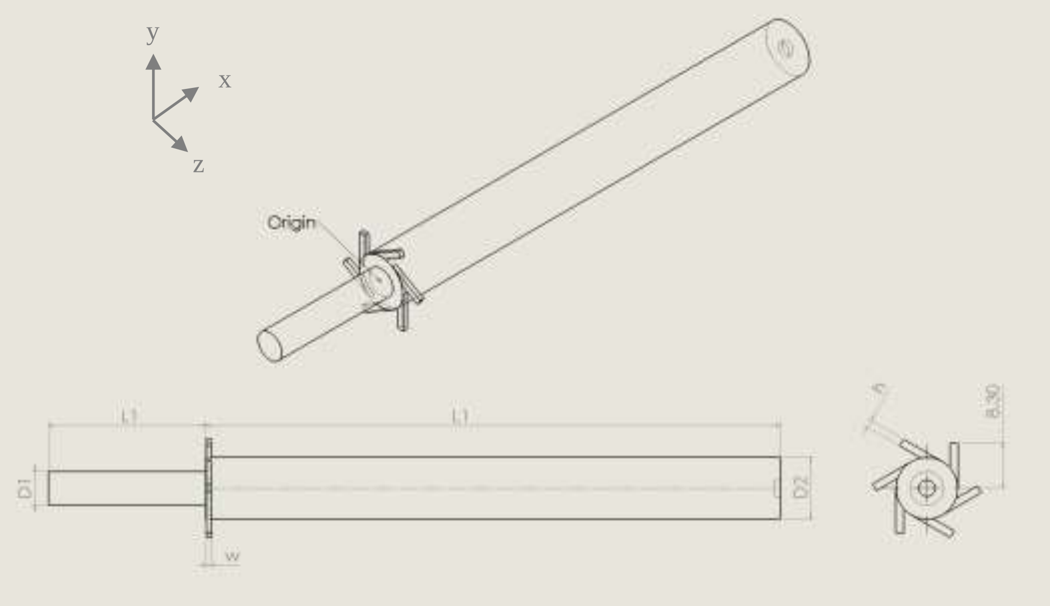

Figure 1. Vortex Tube Geometry

Table 1. Dimensions of Vortex Tube

Geometry	**Value**	**Units**
Inlet height (h)	1.41	mm
Inlet width (w)	0.97	mm
Inlet length (L_0)	8.3	mm
Working tube length (L_1)	106	mm
Working tube diameter (D_1)	11.4	mm
Hot exit area (A_1)	95	mm^2
Cold exit diameter (D_2)	6.2	mm^2
Cold tube length (L_2)	29	mm
No. of inlets	6	

Mesh

In general, there are two types of meshing strategies: Structured and Unstructured. An unstructured mesh has the meshed cells (usually tetrahedrons) randomly distributed across the flow domain. The distribution of the cells will vary with the different algorithms used (e.g. Delaunay triangulation, Octree method, etc.). On the contrary, a structured mesh has the same distribution of cells (hexahedrons) from the starting face and extending through the length of the computational domain. It is this reason why structured meshes are also referred to as swept meshes. They both have their own advantages and disadvantages with respect to the numerical results, convergence, computational time and ease of mesh generation. For example, the unstructured mesh is easier to generate and saves time in the overall process but lacks the ability to be controlled and modified in specific regions in the flow domain. On the contrary, a structured mesh is more difficult to generate but once generated can be easily modified wherever necessary. In the present study both the meshes were compared.

ICEM CFD which is a commercial meshing package available from ANSYS was used for meshing in the current study. The unstructured mesh (Figure 2) was generated using the Delaunay triangulation type mesh generation algorithm. This ensures mesh elements of uniform size throughout the domain. The mesh was then exported to ANSYS FLUENT and converted to Polyhedral cells using the built-in algorithm. The Structured mesh (Figure 2) on the other hand was generated using mapped block meshing method. In this approach, the 3D model was divided into hexahedral blocks which ensured proper connectivity throughout the mesh. This is the phase that requires a significant amount of time as the blocking gets more difficult as the model complexity is increased. But once this process is complete, the mesh can be controlled with ease and modified in the different regions of the domain without much effort. It is also known that for the same number of cells, a structured mesh is runs faster than an unstructured mesh because of the way the numerical algorithm works, which is another advantage of the structured mesh and the reason for choosing it in the current study.

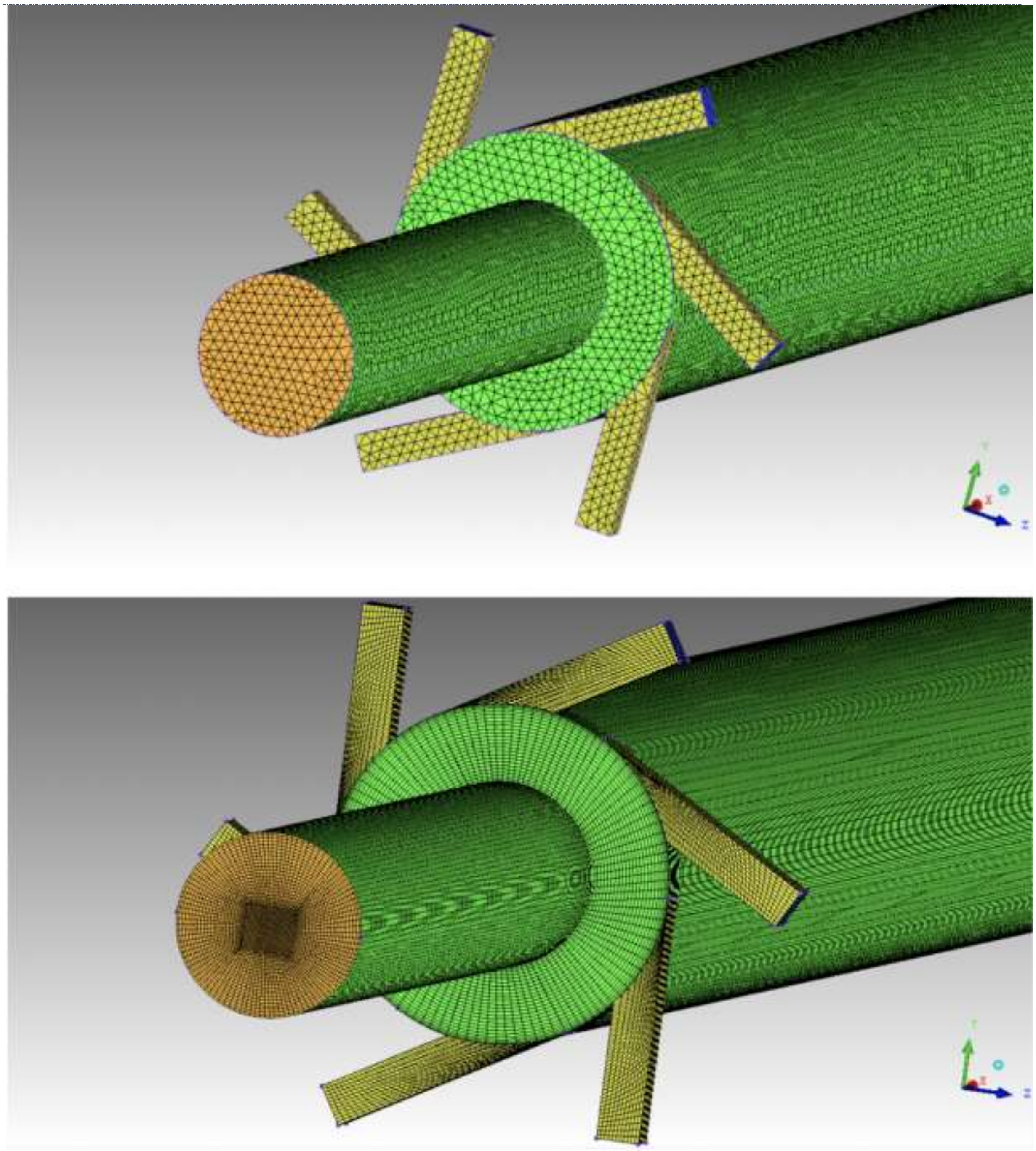

Figure 2. Unstructured Mesh (above), Structured Mesh (below)

Turbulence model

Since this is a study using RANS based turbulence models, the $Std\ k-\epsilon$ model has been chosen for the current study since most of the computational studies have used this turbulence model or a modification of this model. The three most fundamental equations in Computational Fluid Dynamics are the Continuity, Momentum (also referred to as the Navier Stokes eqs.) and Energy equations. All flows must obey these equations in a control volume whose simplified forms are given below:

$$\frac{\partial u_j}{\partial x_j} = 0 \qquad \text{(i)}$$

$$\frac{\partial \rho u_i}{\partial t} + \frac{\partial}{\partial x_j}\left(\rho \bar{u}_i \bar{u}_j + \rho \overline{u_i' u_j'}\right) = -\frac{\partial \bar{p}}{\partial x_i} + \frac{\partial}{\partial x_j}\left[\mu\left(\frac{\partial \bar{u}_i}{\partial x_j} + \frac{\partial \bar{u}_j}{\partial x_i}\right)\right] \quad \text{(ii)}$$

$$\frac{\partial \rho e}{\partial t} + \frac{\partial \rho e u_i}{\partial x_i} = k\frac{\partial^2 T}{\partial x_i^2} - \frac{\partial p u_i}{\partial x_i} + \frac{\partial \tau_{ji} u_i}{\partial x_i} + \rho f_i u_i + \rho \dot{q} \quad \text{(iii)}$$

The equations given above are in time averaged form with the momentum equation carrying extra terms that arise out of the averaging process. Since the averaging process was first done by Osborne Reynolds, they are called referred to as the Reynolds Averaged Navier Stokes (RANS) equations. The term $\rho\overline{u_i' u_j'}$ is the Reynolds stress tensor which contains the information on turbulence and has nine unknowns. Since the number of unknowns exceeds the number of equations, we have what is called as a closure problem. Hence, new equations have to be modelled to compute the unknowns. The following equation is used to model the Reynolds stresses:

$$-\overline{u_i' u_j'} = \mu_t\left(\frac{\partial \bar{u}_i}{\partial x_j} + \frac{\partial \bar{u}_j}{\partial x_i}\right) - \frac{2}{3}k\delta_{ij} \quad \text{(iv)}$$

Here for conceptual simplicity, the turbulent stresses are treated like viscous stresses. Similar to molecular viscosity in viscous stresses, the turbulent or eddy viscosity acts as the proportionality factor between the Reynolds stresses and the strain rate, but with the distinction that it is a property of the flow rather than the fluid itself. The eddy viscosity equation for the $k - \epsilon$ is given as follows:

$$\mu_t = \varrho C_\mu \frac{k^2}{\epsilon} \quad \text{(v)}$$

Where C_μ= 0.09 is a constant [12]. k & ϵ have their own transport equations with different sets of constants that have been found by data fitting numerous classes of turbulent flows and this is the reason why these models are also called as semi-empirical models. The transport equations of k & ϵ are given below:

$$\frac{\partial}{\partial t}(\rho k) + \frac{\partial}{\partial x_i}(\rho k u_i) = \frac{\partial}{\partial x_j}\left[\left(\mu + \frac{\mu_t}{\sigma_k}\right)\frac{\partial k}{\partial x_j}\right] + P_k + P_b - \rho\epsilon - Y_M + S_k \quad \text{(vi)}$$

$$\frac{\partial}{\partial t}(\rho \epsilon) + \frac{\partial}{\partial x_i}(\rho \epsilon u_i) = \frac{\partial}{\partial x_j}\left[\left(\mu + \frac{\mu_t}{\sigma_\epsilon}\right)\frac{\partial \epsilon}{\partial x_j}\right] + C_{1\epsilon}\frac{\epsilon}{k}(P_k + C_{3\epsilon}P_b) - C_{2\epsilon}\rho\frac{\epsilon^2}{k} + S_\epsilon \quad \text{(vii)}$$

Where P_k term represents the production of turbulent kinetic energy and P_b represents the effect of buoyancy. $C_{1\epsilon}$, $C_{2\epsilon}$, $C_{3\epsilon}$, σ_k&σ_ϵ are constants and have the values of 1.44, 1.92, -0.33, 1.0, 1.3 respectively.

Boundary conditions and numerical method

The boundary conditions used in the current study are listed in the following table and referenced to the boundaries of the computational domain.

Table 2. Boundary Conditions

Computation Boundaries	Boundary Condition	Value
Inlet	Pressure inlet	570,168 *Pa*, 294 *K*
Hot exit	Pressure outlet	Varied to get different Cold Mass Fractions (ε)
Cold exit	Pressure outlet	101,325 *Pa*
Walls	Adiabatic wall with no slip	Heat Flux = 0 W/m^2

*All pressure values are absolute values since the operating pressure was set to 0 Pa.

Since this is a compressible flow problem and the flow variables are highly coupled, density based implicit solver was chosen with the ideal gas equation ($P = \rho RT$) to model the pressure, temperature and density. The operating pressure was set to 0 Pa and hence all the pressure values were given as absolute values as this is the general convention followed during compressible flow simulations. Turbulent intensity and turbulent viscosity ratio were set at default values of 5% and 10 respectively at the inlet. Second order upwinding scheme was chosen for all the flow variables and all other under relaxation factors were left with default values. Convergence was monitored in three ways:

(1) All the residuals (continuity, momentum, energy, k & ϵ) were allowed to reach an order of 10^{-6}.
(2) Mass weighted average total temperatures at the hot and cold exit were allowed to asymptote.
(3) Mass flux difference was monitored between the inlet and the outlets until it reached a value of the order of 10^{-6}.

If issues were faced regarding convergence, then the Courant number was reduced (usually from 5 to 1) and then the simulation was rerun.

4. VALIDATION

As mentioned earlier, the Skye et al. model [11] was used for validation. The results of the validation are shown in Figure 3 & Figure 4. In their work [11] the authors calculated the non-dimensional energy balance error and found this error to be more than 10% for cold mass fractions on both the extreme ends (high and low). Since the Cold mass fractions in the range of 0.18 - 0.82 had less than 5% error in the energy balance, they were the ones used to compare the computational results with. Cold mass fraction (ε) is the ratio of the mass flow rate exiting the cold exit to the mass flow rate entering the vortex tube at the inlet. The current CFD results appear to show good agreement with Skye et al. [11] experimental results. Specifically the Hot exit temperature agrees within 10 % over the tested cold mass fraction range and likewise for the Cold exit temperature as well thus providing confidence in the current CFD model.

Since the current CFD model using an unstructured mesh was validated, the runs were repeated with structured mesh. The structured mesh was run for single case with a Cold Mass Fraction (ε) of 0.52. This case was chosen not for any particular reason but because this one lies in the middle of the cold mass fraction range. The total temperature at the hot and cold exit were compared and found to be in good agreement with the validation case. In fact, the current computation agreed better with Skye et al. [11] experimental results, than their own computations. Grid sensitivity was then done with the structured mesh as the results from the structured mesh were used for the analysis. The results are shown in Figure 5.

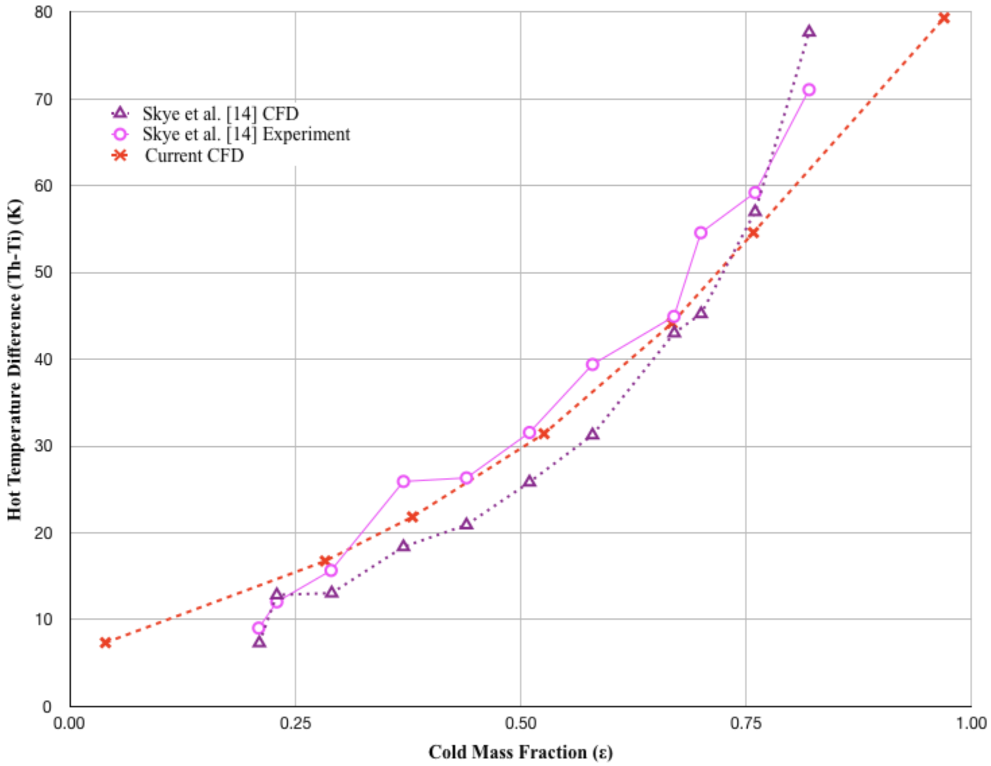

Figure 3. Hot Temperature difference for various Cold Mass Fractions

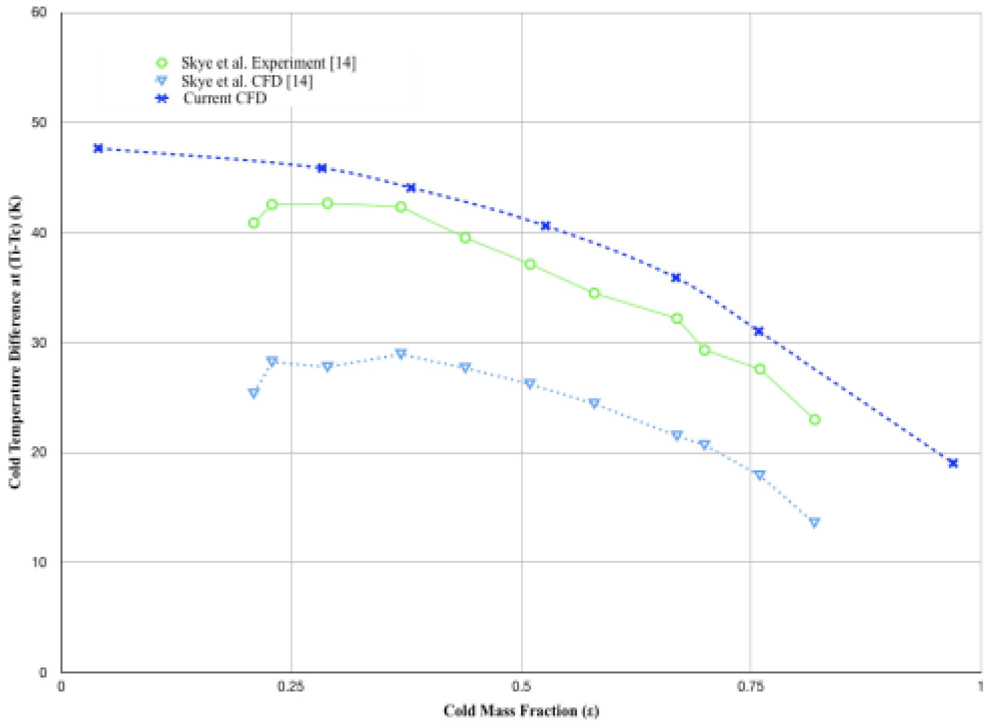

Figure 4. Cold Temperature difference for various Cold Mass Fractions

Once the validation was done, the valve at the hot end was modified as the hot exit area from the Skye et al. [11] model used for validation was large and caused some convergence issues after mesh refinement because of backflow occurring at the hot exit. Hence, the hot valve geometry was modified for further analysis using the hot valve dimensions from the vortex tube model used in Rajagopalan's study [8] and all the other dimensions were kept the same from the model used for validation. This change didn't produce much difference in the total temperatures and this model was the one used for further analysis.

5. GRID SENSITIVITY

Since the computational results depend on the grid domain and the number of elements, as the number of elements increases, the accuracy of the solution also increases. But care should be taken as to not over refine the mesh which might decrease the mesh quality in some areas and can cause some solution non-linearities to intensify which can cause the solution to not converge, as well as unnecessarily increase the computational costs. As it can be seen in Figure 5, the total temperatures asymptote at 3.2 million cells and shows no further change with an increase in the number of cells thus becoming grid insensitive at this point. However, when the Reynolds stress was monitored for grid sensitivity (Figure 6) solution became grid independent at 3.2 million cells. The background and the procedure for the calculation of the Reynolds Stresses is explained in a later section in this paper. It can be seen that the curves for Reynolds Stress Vs Radius shown in Figure 6 for different grids fall on top of one another. Note, for each of the visible curves in Figure 6 there are three curves that makeup that line showing all the three meshes produce the exact same results.

Although the Grid Convergence Index (GCI) is the latest advancement in evaluating the effectiveness of the grid refinement process, it was not utilized in the current study. This was a result of parameters which were being monitored i.e. Total Temperatures and the Reynolds Stresses showed insignificant changes with the different meshes used in our study.

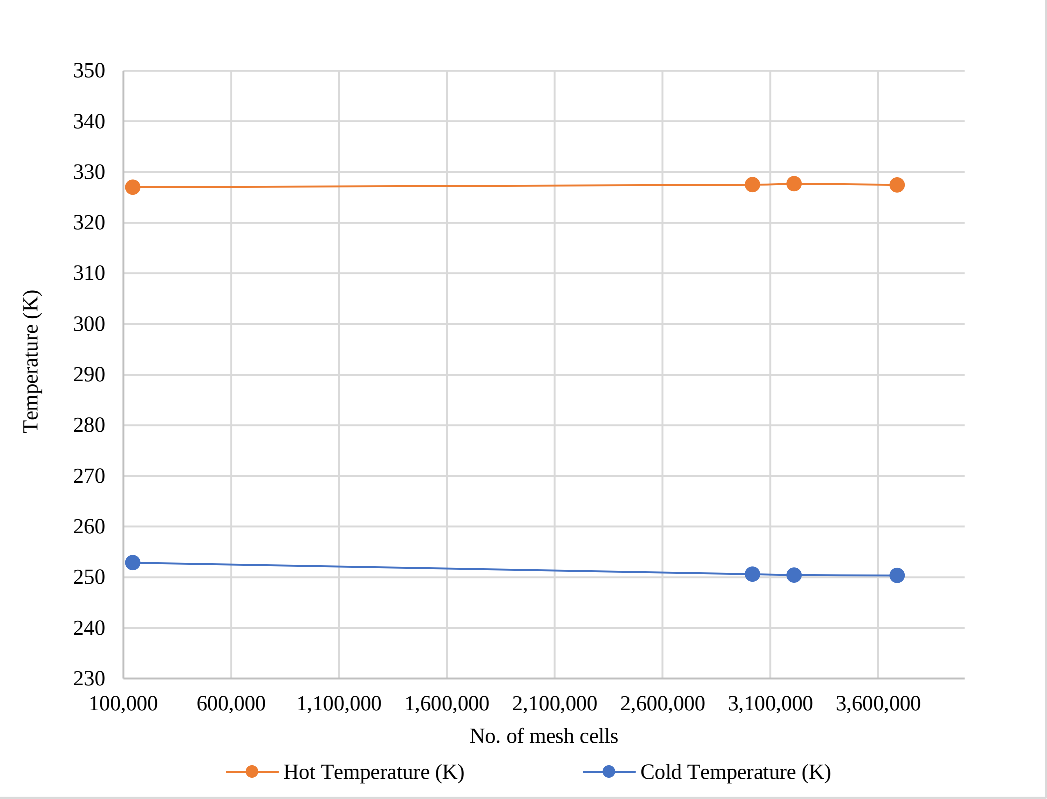

Figure 5. Grid sensitivity test

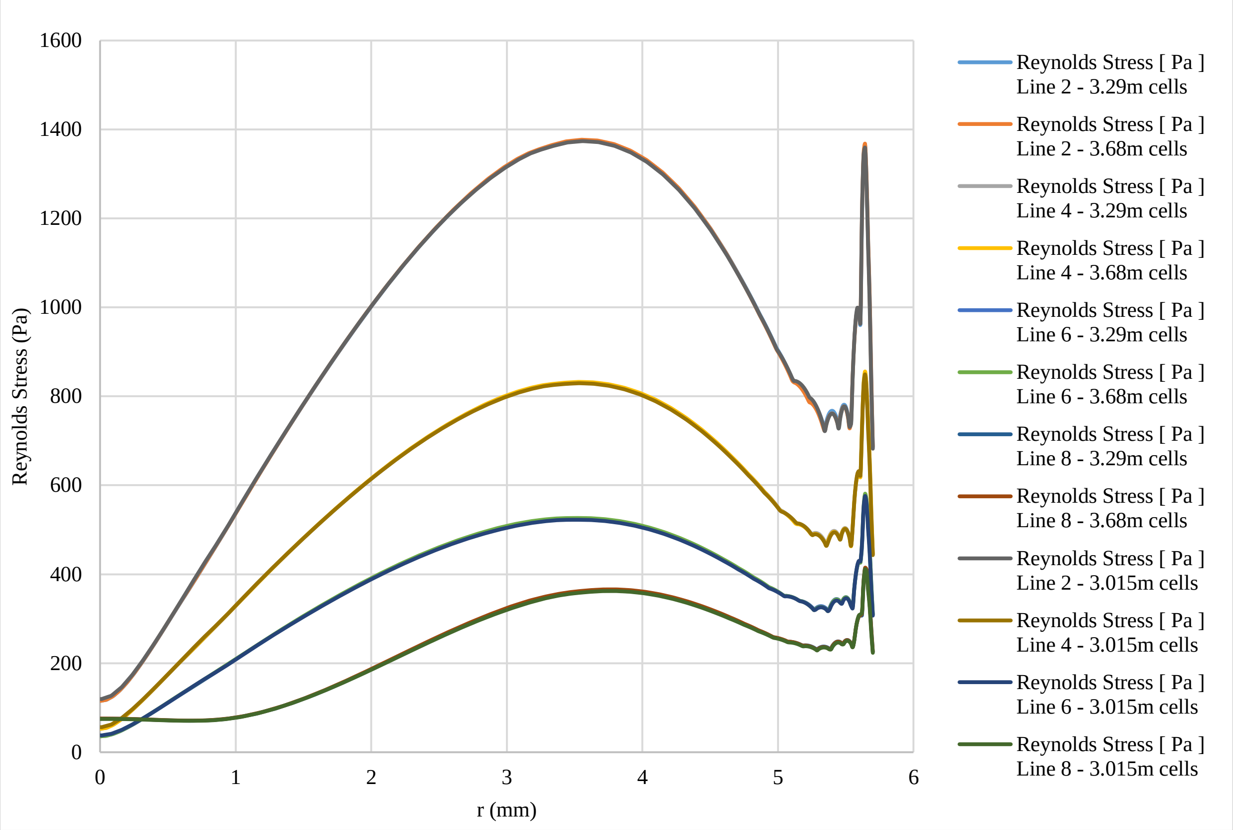

Figure 6. Grid sensitivity test on hexahedral mesh based on Reynolds Stress

In the above chart, Line 2, 4, 6, 8 refers to the axial locations x = 20 mm, 40 mm, 60 mm, 80 mm respectively.

6. ANALYSIS

The current analysis was performed in two separate phases:

(i) In the first phase the velocity and temperature profiles were compared to a published Large Eddy Simulation (LES). This data provided a comparitive data set for the present research and a baseline for evaluations ofthe RANS models employed in the current work as well as hightlight the similaritiesand differences.

(ii) In the second phase of this study, the results of a well documented flow field are provided and will be used in the next phase of this effort to better understand the energy separation phenomenon.

Comparison with LES research

In the following section the current Tangential, Axial velocity and Static Temperature profiles at two downstream stations computed using a RANS approach are compared to the published LES data by Secchiaroli et al. [7]. Radial velocity profiles were not shown here because the value of radial velocity is insignificant when compared to the tangential and axial velocities. It is important to note that the work of Secchiaroli et al. [7] is used for qualitative comparison, however since his study was conducted with an inlet Re of only 11,769 (calculated using the inlet geometry) whereas the current simulation utilized an Re = 16,213, their Re number is approximately 40% lower and believed to account for some differences.

Comparison of Tangential Velocity Profiles

The velocity magnitude and its components provide insight into the type of flow within the vortex tube. Since the flow within the confined vortex chamber is swirling, a Rankine vortex structure can be expected as suggested by previous research [3]. In a Rankine vortex, the inner core of the flow has a forced vortex structure where the tangential velocity is proportional to the radius ($w \propto r$) and there is no relative motion between the fluid layers. This is also referred to as a region of solid body rotation. Beyond this radial location the flow transitions to a free vortex. After the transition region, there is the free vortex with tangential velocity inversely proportional to the radius ($w \propto 1/r$). Generally, the free vortex region has a hyperbolic velocity profile with an equation $w \propto Cr^{-\alpha}$ where α varies from 0.71 to 0.78 [13].

In addition to LES, Secchiaroli et al. [7], also used an RSM (Reynolds Stress Model) and $RNG\ k-\varepsilon$ and they reported the tangential, axial velocity and static temperature profiles at different axial locations along the vortex tube. Due to the differences in geometry and the resulting interference of the hot exit valve only two axial locations could be compared to our current study. These axial locations were equivalent to x=36 mm and x=56 mm in the present CFD simulations.

The normalized tangential velocity profiles are compared in Figure 7 & Figure 8. Velocity Normalization was performed by dividing the local velocity by the maximum velocity calculated by each model. Likewise, the normalized radius was determined by dividing the local radial position by the tube radius.

From the Figure 7, it can be seen that the tangential velocity computed by the $Std\ k-\epsilon$ model is qualitatively different from LES and $RNG\ k-\varepsilon$ models. Using a +/- 5% as a indicator and estimating the various region the Std. $k-\epsilon$ model predicts a forced vortex zone extending from the center to y/R of 0.7 and a transition zone up to y/R of 0.92 where the velocity stars to drop. The LES predicts a forced vortex region from the center to y/R of 0.26 and a transition zone up to y/R of 0.6 and then the velocity starts to drop as we move towards the annular region.

But in the case of the x=56 mm shown in Figure 8, $Std\ k-\varepsilon$ model produces similar results to the $RNG\ k-\varepsilon$, but these are again very different from the ones given by the LES which predicts a hyperbolic velocity profile which corresponds to a free vortex flow all the way from y/R of 0.5 and a transition from forced vortex around y/R of 0.2. Since the $RNG\ k-\varepsilon$ is a modification of the Std. $k-\varepsilon$ model and is theoretically said to give improved results for rotating flows, strain dominated flows [14] because of the way in which the eddy viscosity is modelled to take into account the effects of swirl. The $RNG\ k-\varepsilon$ thus produces a decent agreement with LES in the region closer to the inlet where the swirl intensity is higher and produces results similar to the Std. $k-\varepsilon$ at further axial distances as the swirl gets weaker.

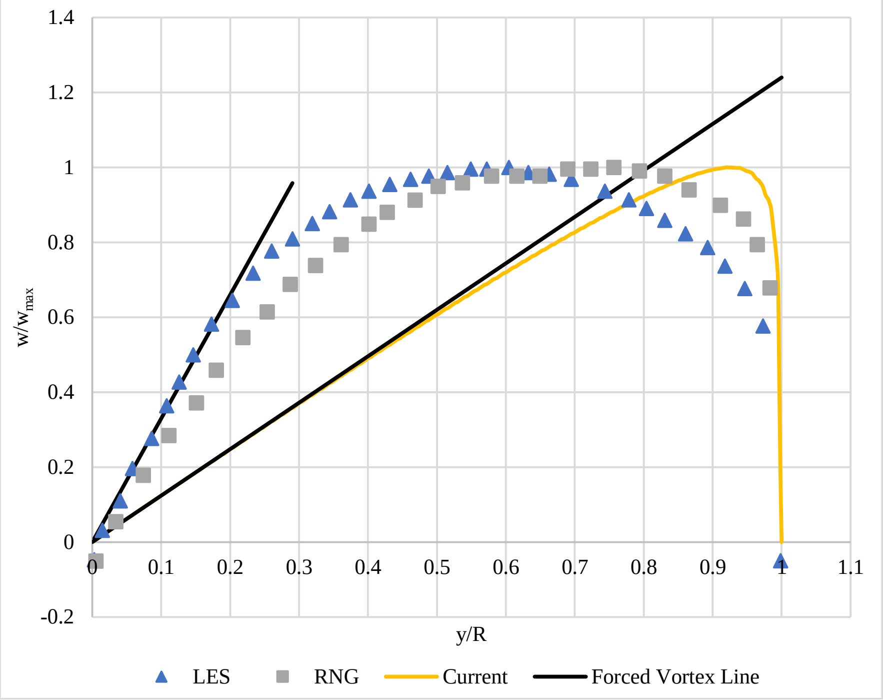

Figure 7. Normalized tangential velocity at x=36 mm

This result from the Std. $k-\epsilon$ model is along expected lines as it has been shown in previous works [15,16] that the eddy viscosity models like Std. $k-\epsilon$ which use a Boussinesq approximation for the Reynolds Stresses tend to neglect the anisotropic distribution of the normal stresses (u'^2, v'^2, w'^2) that arise in swirling flows. The eddy viscosity models also fail to take into account the damping of the turbulent stresses due to swirl and this is turn causes them to predict an overly diffusive flow-field which reflects in the prediction of the tangential velocity profiles.

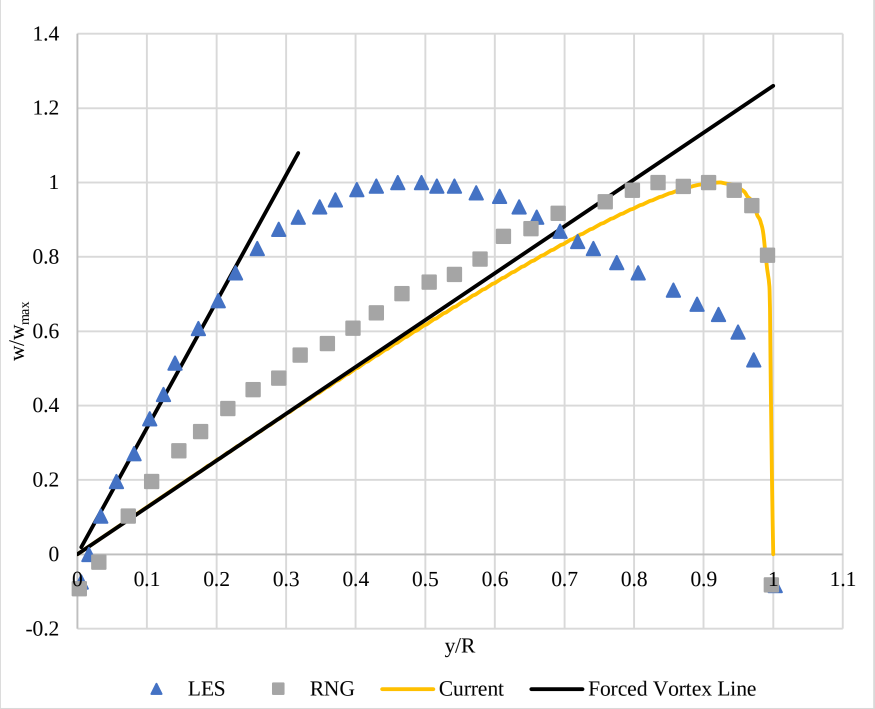

Figure 8. Normalized Tangential Velocity at x=56 mm

Comparison of Axial Velocity Profiles

Examining the Normalized Axial velocity profiles from Figure 9 & Figure 10, the $Std\ k-\varepsilon$ model appears to predict the cross-over point i.e. the region where axial velocity is zero, with a reasonable accuracy when compared with other models. $Std\ k-\varepsilon$ model predicts an almost linearly increasing axial velocity profile from the cross-over point to the annular region whereas the LES and RNG predict a qualitativey different behaviour. However, at the core the LES shows a region of flow oscillation in the forced vortex and the likelihood of a non-uniform flow in the core region. The $RNG\ k-\varepsilon$ model which has a near one to one agreement in the free vortex region of the flow and is completely off in the forced vortex core and overpredicts the axial velocity by an extremely large margin below a y/R of 0.35. The $Std\ k-\varepsilon$ on the other hand has a reasonable agreement with LES in the core region with the exception of the oscillation found in LES at y/R of around 0.3.

At x=56 mm, a similar trend can be observed. All the models agree well in terms of the cross-over region and also show a similar behavior as the previous case above the cross-over region towards the annular region. Again in the core region, the $RNG\ k-\varepsilon$ tends to overpredict the axial velocity but the $Std\ k-\varepsilon$ has a reasonable agreement with the LES model.

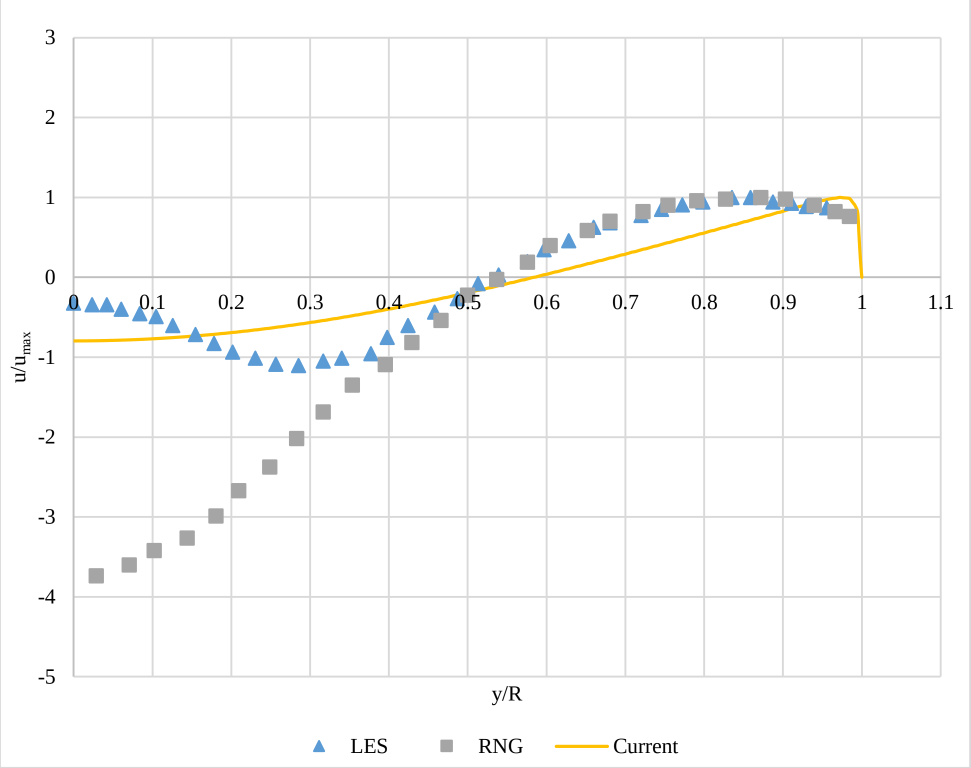

Figure 9. Normalized Axial Velocity at x=36 mm

Comparison of Static Temperature Profiles

The normalized static temperature profiles have also been compared in Figure 11 & Figure 12. Normalization was done by dividing the static temperature at each point by the maximum static temperature at that axial location.

The $Std\ k - \varepsilon$ model shows an almost constant static temperature profile from the core all the way to a y/R of 0.9 and starts to increase at the wall. LES shows a drop-in temperature around y/R of 0.3 where the drop in axial velocity was observed and shows an almost linear increase in temperature all the way to the wall. The model again agrees well from the transition region into the free vortex region, but overpredicts the temperature drop in the forced vortex region below a y/R of 0.3. A possible reason might be the high axial velocities that the $RNG\ k - \varepsilon$ model predicts in the core which tends to a lower pressure and ultimately lower temperatures.

A similar trend can be observed in the case of x=56 mm but the maximum differences between the normalized values have gone down to about 3.5%.

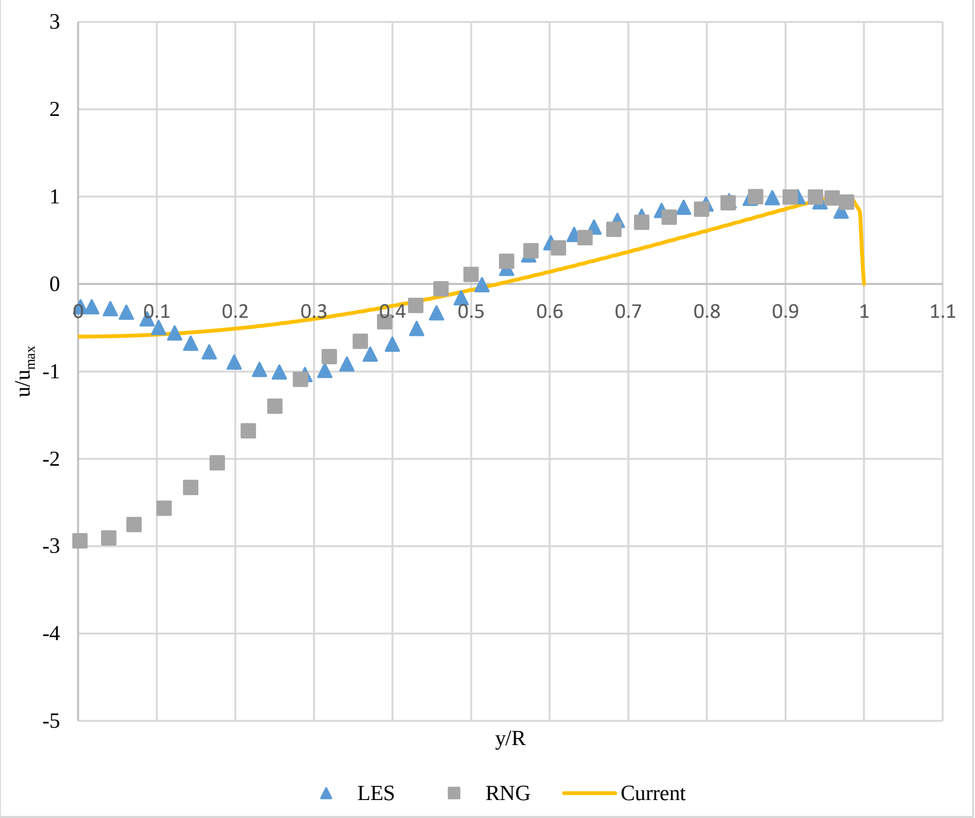

Figure 10. Normalized Axial Velocity at x=56 mm

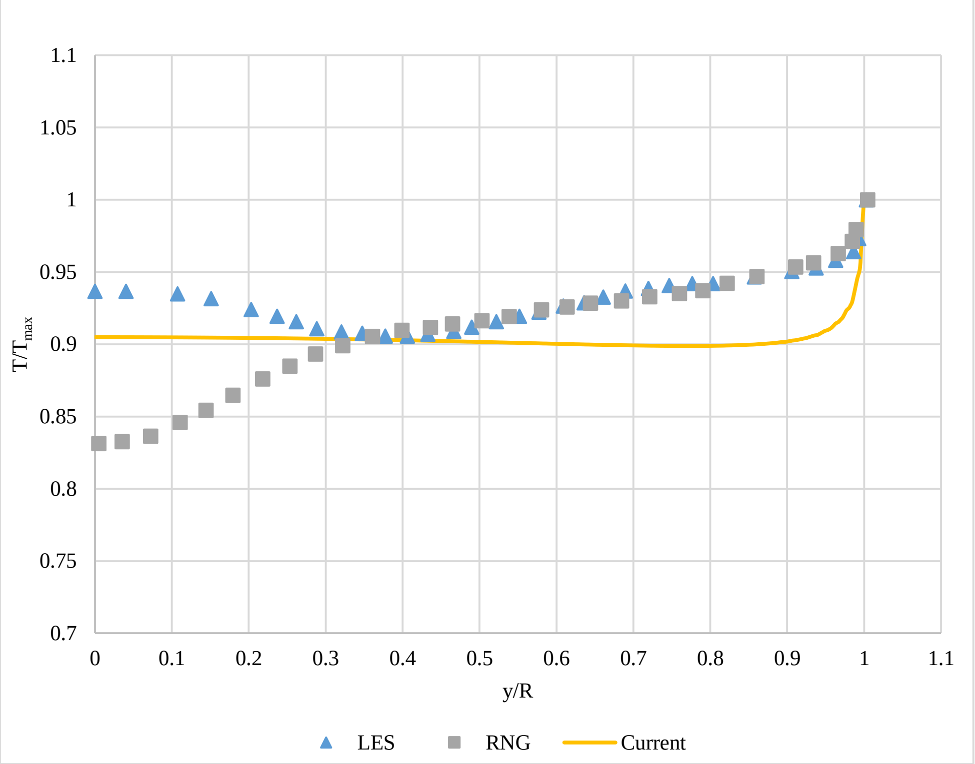

Figure 11. Normalized Static Temperature at x=36 mm

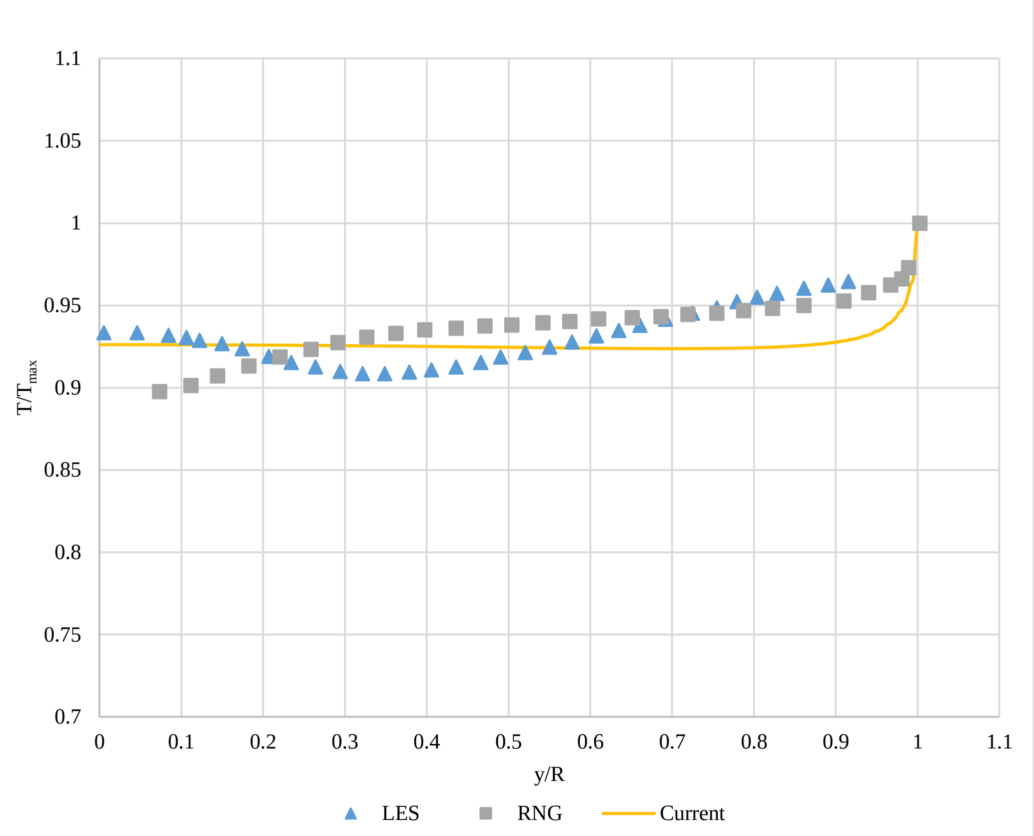

Figure 12. Normalized Static Temperature at x=56 mm

A qualitative comparison of the flow i.e. the normalized tangential velocity, axial velocity and the static temperature profiles was made with a published research using a higher order model and the following observations have been noted:

(i) The $Std\ k-\varepsilon$ model predicts a qualitatively different distribution of a Rankine vortex when compared to the LES simulation. It is belived this is due to the way in which the eddy viscosity is modelled which does not take into account the effects of swirl on the mean flow.

(ii) The axial velocity profiles predicted by the $Std\ k-\varepsilon$ model agree fairly well with the LES in the core region and also the location of the cross-over between the counter-flowing streams.

(iii) The Static Temperature profile predicted by $Std\ k-\varepsilon$ is almost flat in the central regions of the tube and shows an increase in the region near the tube wall.

Having an idea of the various benefits and the shortcomings of the Std. $k-\varepsilon$ model, an analysis of other flow parameters inside the vortex tube were performed.

Analysis of the results from the current simulation

Stations chosen to study the results

The current vortex tube simulations and the corresponding analysis of the results have all been performed in the Cartesian Coordinate system and the results are converted to a Cylindrical Coordinate system when needed. The origin (x, y, z = 000) is located along the vortex tube center line and at the plane of junction between the vortex tube main cylinder (right hand side of the origin) and the cold exit tube (left hand face). The orientation of the vortex tube with respect to the coordinate system and the location of the origin can be seen in Figure 13.

Since the flow within the vortex tube is highly three-dimensional, all the three components of velocity i.e. the tangential, radial and the axial components (w, v, u) within the vortex tube hot section were examined. Radial lines represent the downstream locations where the computational results (Figure 14) are presented. These locations are x = 5mm, 10 mm, 20 mm, 40 mm, 60 mm and 80 mm. Beyond the 80 mm downstream from the nozzle inlet is the hot exit control valve surface, which begins to interfere with the flow therefore no axial locations beyond the 80 mm were considered in the current study.

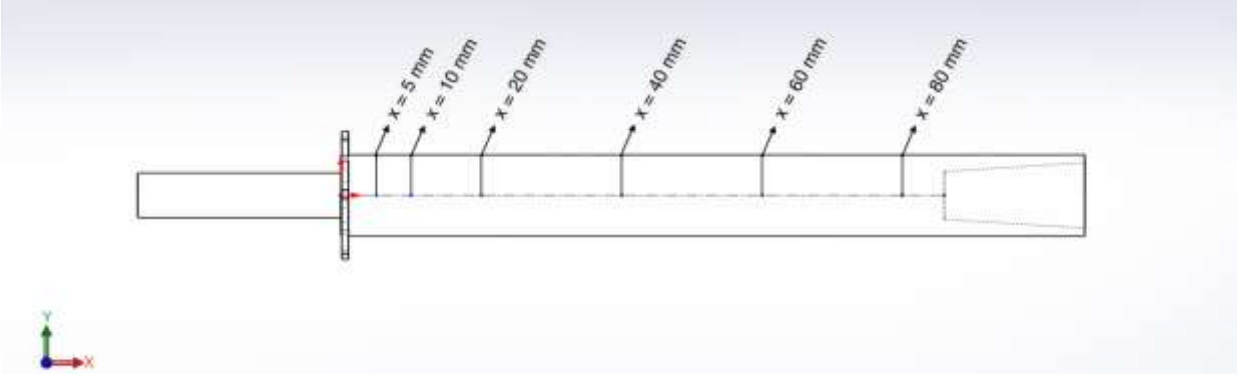

Figure 13. Result stations in the current model

Velocity Analysis

Figure 14 shows the tangential velocity distribution from the current simulation. As seen in the above comparisons, the velocity profiles show an increasing magnitude towards the wall. The velocity starts to drop at a radial location of approximately 5.35 mm (except at x=5 mm) signaling a start of transition region which eventually turns into the free vortex region and reaches zero speed at the wall because of the no slip condition imposed by the wall boundary condition.

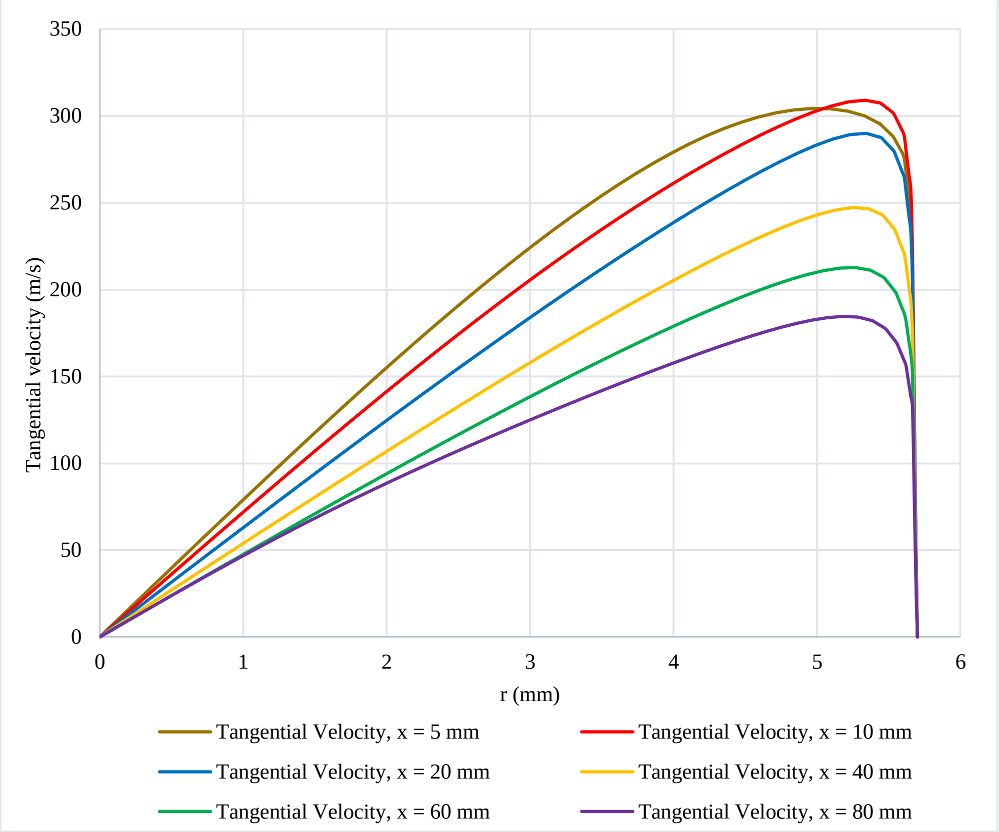

Figure 14. Tangential velocity distribution at various cross sections

In order to differentiate between the hot and the cold flow at the various sections, the axial velocity profiles are studied. In the current orientation of our vortex tube, a negative axial velocity signifies flow moving towards the cold end and a positive axial velocity signifies flow moving towards the hot end. It can also be seen that the radial location of the flow reversal decreases as we move towards the hot end in Figure 15. If all the cold flow has reversed at a particular axial location where we see a zero axial velocity at the centerline and no negative axial velocities beyond this point, then this is called as the stagnation point. Previous vortex tube studies have shown that the maximum total temperature of the annular flow can be observed at the axial location where this stagnation point is located and that the total temperature does not increase further beyond this region. However, presence of such a stagnation point was not observed in the current study due to the geometry and conditions used for the vortex tube.

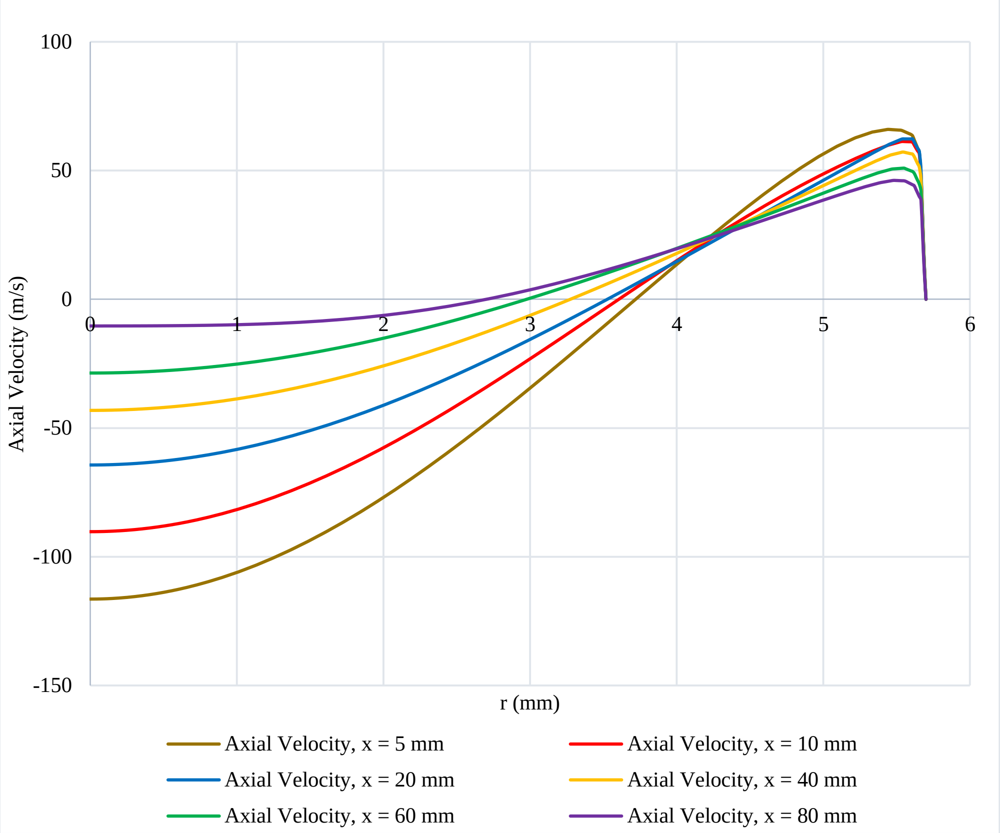

Figure 15. Axial velocity at various axial locations

Figure 16 shows the location of the zero axial velocity i.e. the interface between the two flows at various axial locations along the tube. From this it can be seen that the flow reversal region keeps shrinking as we move towards the hot exit. The movement of the interface location towards the centerline shows a linear trend (shown in the R^2 value for linear fit) as we move downstream from the inlet.

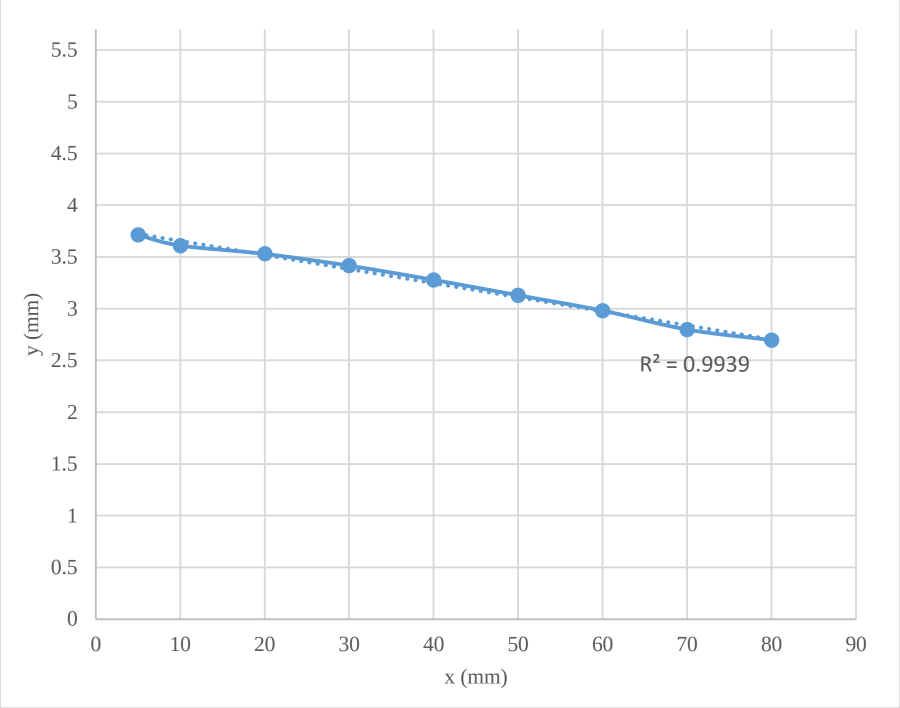

Figure 16. Zero axial velocities at different axial locations

Vorticity and Strain rate

The two important parameters that are also addressed in the current analysis are the Vorticity and the Strain Rate. If we imagine a fluid packet to be a cube present in the fluid flow and the flow to be a collection of such fluid packets, then these are the two effects that the fluid packet undergoes in a flow and together they make up the deformation tensor. Vorticity is the rate at which the fluid packet i.e. the cube rotates, and the strain rate is the rate at which the fluid packet undergoes deformation in the form of shear.

$$\frac{\partial U_i}{\partial x_j} - Deformation\ tensor$$

$$\frac{\partial U_i}{\partial x_j} = \frac{1}{2}\left(\frac{\partial U_i}{\partial x_j} + \frac{\partial U_j}{\partial x_i}\right) + \frac{1}{2}\left(\frac{\partial U_i}{\partial x_j} - \frac{\partial U_j}{\partial x_i}\right) \quad \text{(viii)}$$

where, $s_{ij} = \frac{1}{2}\left(\frac{\partial U_i}{\partial x_j} + \frac{\partial U_j}{\partial x_i}\right)$ - Symmetric part (or) Strain rate

$\omega_{ij} = \frac{1}{2}\left(\frac{\partial U_i}{\partial x_j} - \frac{\partial U_j}{\partial x_i}\right)$ - Skew-symmetric part (or) Vorticity

A constant vorticity with no shear should be expected in the forced vortex region. In the free vortex region, the vorticity should go towards zero as the free vortex flow is irrotational. The Figure 16 shows the Axial Vorticity (Vorticity X in current simulation) in various axial locations downstream of the nozzle inlet. The vorticity changes considerably in the axial locations at 5 mm and 10 mm with the forced vortex region being very small. Further downstream, at other axial locations (20, 40 & 60 mm), the vorticity remains fairly constant in the central regions with the gradient being small in the forced vortex region and then dropping to a zero magnitude in the annular region, only to increase because of the boundary layer effects close to the wall. Again, at x = 80 mm, the vorticity curve shows considerable change even close to the center and this can be attributed to the presence of the hot valve which causes disturbances to the flow as this axial location lies very close to the hot valve.

The vorticity changes by approximately 9% from the tube centerline to the location where the axial velocity goes to zero at a stream wise i.e. axial location of x=20 mm. Since we know that the core flow is a forced vortex flow, we have fixed the condition that any change in vorticity less than 10% will be considered as approximately constant and thus represent the forced vortex zone. This agrees with other locations as well (x=40 & 60 mm).

Strain rate reported here is directly output from ANSYS Fluent which defines strain rate as the second invariant of the deviatoric stress tensor. Hence, strain rate is the rate of shear deformation the fluid packet undergoes. Strain rate plot is shown in Figure 17 and it can be observed that the strain rate is very low in the core flow which is the forced vortex flow. It then increases and has an inflection point at around radius of 3 mm if we look at the x=10-, 20- and 40-mm curves where the gradient of the rise drops. It then has another inflection point at radius of 5 mm from where it starts increasing exponentially towards the annular region reaching very high values near the wall.

To calculate the Reynolds Stress which is the production of stress due to turbulent momentum transfer in the fluid, the Boussinesq equation is invoked. Thus, the Reynolds Stress is calculated here as the Eddy Viscosity (μ_t) times the Strain Rate.

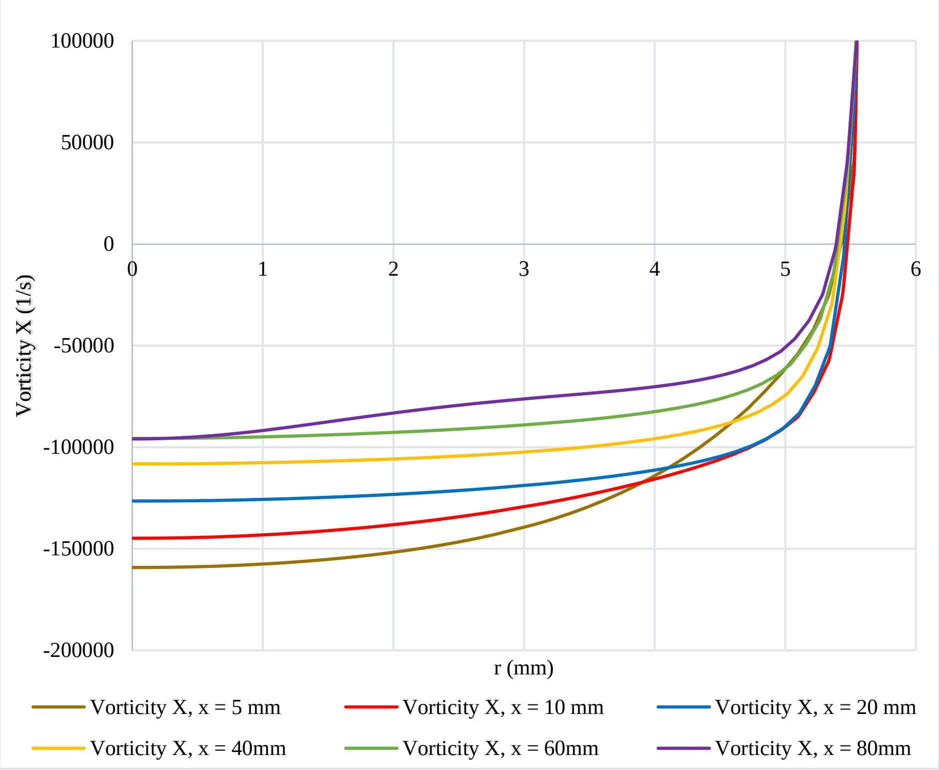

Figure 16. Vorticity X at various locations

One of the drawbacks of the isotropic eddy viscosity models like the $Std\ k-\epsilon$ can be seen here. The eddy viscosity shown in Figure 18 is calculated to be almost uniform from the center to the annular region with the eddy viscosity dropping to zero near the wall. Whereas eddy viscosity should be expected to be low at the core because of the ability of forced vortex to be resistant to the turbulent momentum transfer, then peaking at the region where axial velocity goes to zero because of shear between the two counter-flowing streams and again dropping to zero near the wall [17].

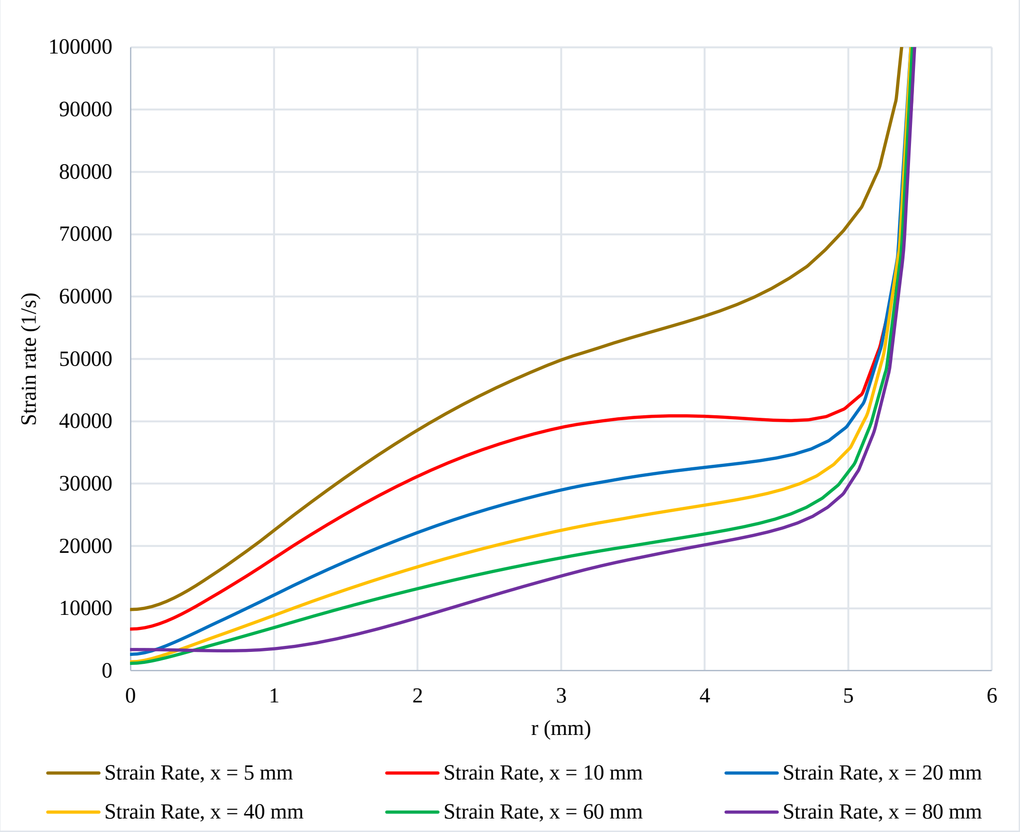

Figure 17. Strain rate at various axial locations

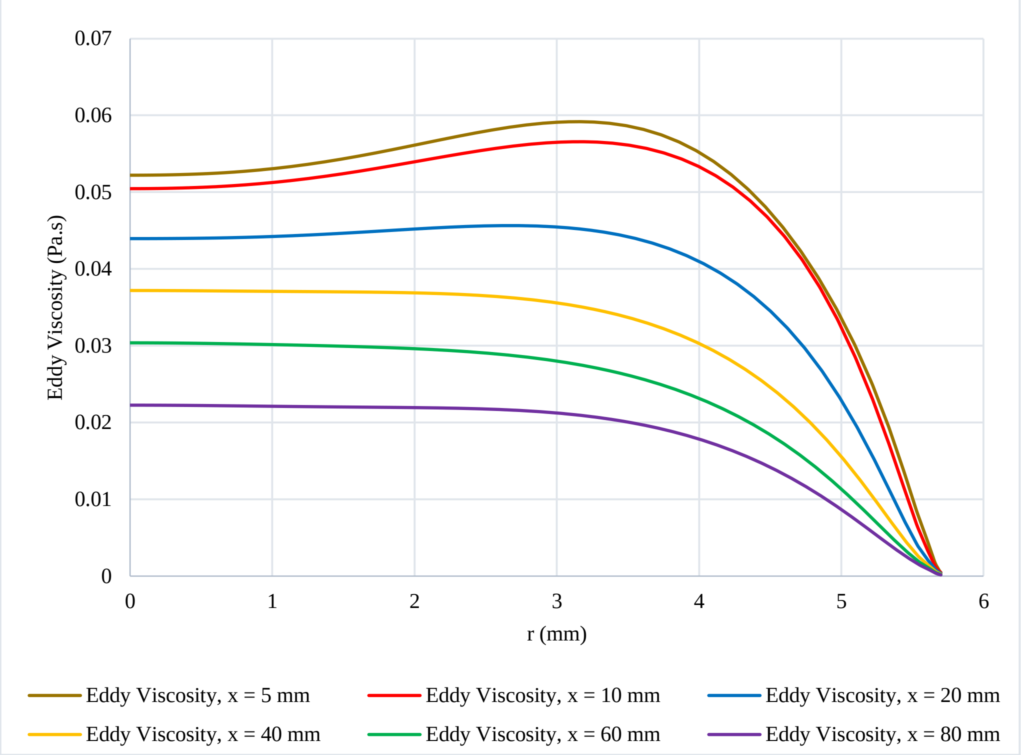

Figure 18. Eddy viscosity at various axial locations

From the Figure 19, we can observe that the Reynolds stress is very low in the core flow and increases with radius and peaking around the center of the radial location. It then starts dropping towards the annular region and has a sudden peak near the wall before dropping to zero at the wall. The overly diffusive profile of the eddy viscosity has resulted in a similar characteristic for the Reynolds Stress. The Reynolds Stress although predicted to be high in the region of the zero-axial velocity can be seen to have a bigger spread than what is normally expected [15].

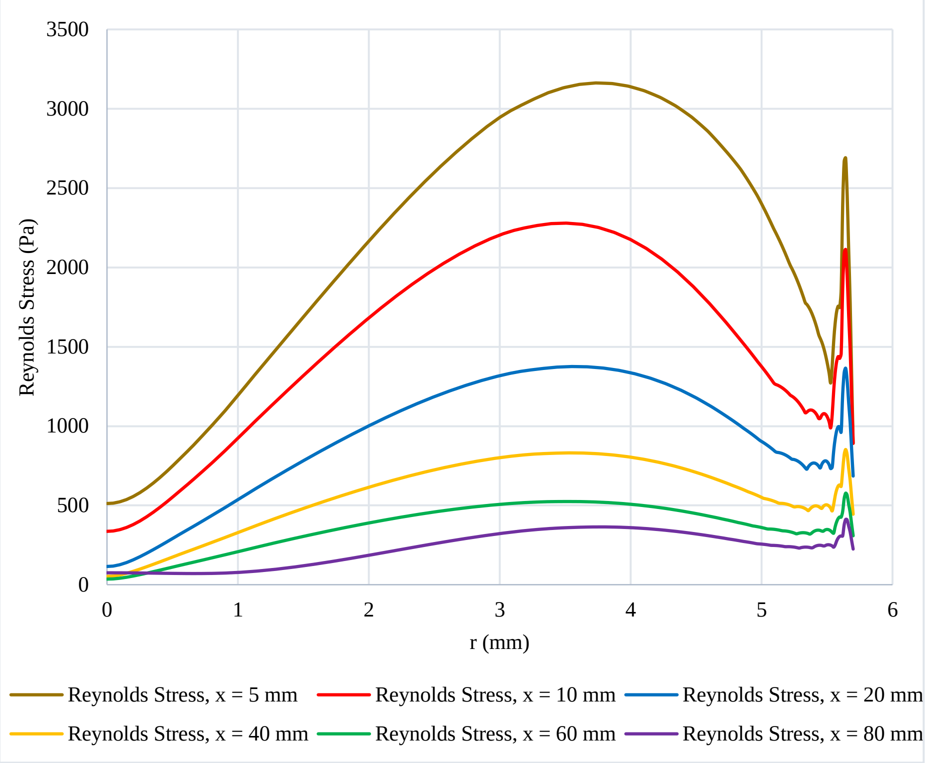

Figure 19. Reynolds Stress at various axial sections

7. SUMMARY

The computational analysis of the properties of the flow inside a counter-flowing Vortex tube has been performed using a RANS based two-equation turbulence model $Std\ k-\varepsilon$. The model was intially validated using experimental results and the agreement was found to be very good in terms of the total temperature predictions at the hot and cold end. Then comparison of the flow properties like the velocity and the static temperature profiles was made with a published computational research which used higher order LES model and thisprovided insight into the differences between the various turbulence models. The $Std\ k-\varepsilon$ predicted a qualitatively different flow profile for the tangential velocity with a different distibution of the free, transition and forced vortex region when compared to the LES. The LES predicted a forced vortex region only upto a radial location y/R of 0.25, then a transition region and a free vortex region whose size with respect to radius increased with an increase in the axial distance from the inlet. Whereas the $Std\ k-\varepsilon$ model predicted a overly diffusive tangential velocity profile with the forced vortex extending upto a y/R of 0.7 and then the free vortex region came very close to the wall at a y/R of 0.92. The behavior was the same for all the axial locations with the magnitude of the tangential velocity itself dropping in further downstream locations. The axial velocities predicted by the LES research had a bit of a non-linear characteristic in both the forced and the free vortex region but the $Std\ k-\varepsilon$ model predicted an almost linearly increasing axial velocity profiles in both the regions. Static temperature profile predicted by $Std\ k-\varepsilon$ remained fairly constant almost in the entire radius at a particular axial location and increased very close to the wall.

Vorticity results from the $Std\ k-\varepsilon$ model confirmed the presence of a forced vortex region at the core with the vorticity being constant in the forced vortex region, dropping to zero in the annular region and then increasing exponentially in the region close to the wall because of the presence of a boundary layer. The strain rate curves showed a very low strain rate in the central region and increasing with the radius. There was a presence of an inflection point in the central regions of the radius where the gradient of the rise dropped and then anotherinflection point appeared at the annular region where the values increased exponentially till the wall. The Reynolds Stress which was calcuated using the Boussinesq hypothesis was found to agree well with our expectations with the presence of high shear in the cross-over region i.e. the interface between the two counter-flowing fluid streams. But it was found to have an overly diffusive profile caused by the eddy viscosity as the Reynolds Stress is a combination of both the eddy viscosity and strain rate. This was expected as the two-equation isotropic models like the $Std\ k - \varepsilon$ are expected to calculate an overly diffusive eddy viscosity profile because they neglect the effect the swirl has on the dampening of the turbulent stresses.

8. NOMENCLATURE

L	Vortex tube length, m
D	Vortex tube diameter, m
y	Radial Coordinate, m
R	Radius of Vortex tube, m
k	Turbulence Kinetic Energy, m^2/s^2
ϵ	Rate of Dissipation, m^2/s^3
ω	Specific rate of dissipation, 1/s
μ	Molecular viscosity, Pa.s
μ_t	Turbulent viscosity, Pa.s
ε	Cold mass fraction, $\frac{\dot{m}_c}{\dot{m}_i}$
u, v, w	Mean velocities in x, y & z-directions
u', v', w'	Instantaneous velocities in x, y & z-directions
ex	Exergy, J
Θ	Exergy Density,$\frac{ex}{ex_{max}}$
ω_{ij}	Vorticity, 1/s
S_{ij}	Strain rate, 1/s
δ_{ij}	Kronecker delta
$\overline{u_i' u_j'}$	Reynolds Stress, Pa
$C_\mu, C_{1\epsilon}, C_{2\epsilon}, C_{3\epsilon}, \sigma_k \& \sigma_\epsilon$	Turbulence model constants

REFERENCES

[1] J. P. Harnett and E. R. G. Eckert, "Experimental Study of the Velocity and Temperature Distribution in a High-Velocity Vortex-Type Flow," American Society of Mechanical Engineers, pp. 751-758, 1957.
[2] H. H. Brunn, "Experimental Investigation Of The Energy Separation in Vortex Tubes," Journal Mechanical Engineering Science, vol. 11, no. 6, pp. 567-582, 1969.
[3] J. C. Chen and C. A. Lin, "Computations of Strongly Swirling Flows with Second-Moment Closures," International Journal for Numerical Methods in Fluids, vol. 30, p. 493–508, 1999.
[4] W. Frohlingsdorf and H. Unger, "Numerical investigations of the compressible flow and the energy separation in Ranque-Hilsch Vortex Tube," International Journal of Heat and Mass Transfer, vol. 42, pp. 415-422, 1999.
[5] J. J. Keyes, "An Experimental study of gas dynamics in high velocity vortex flow," in Proceedings of the Heat Transfer and Fluid Mechanics Institute, Stanford University, Oak Ridge National Laboratory, Tennessee, 1960.
[6] T. Dutta, K. P. Sinhamahapatra and S. S. Bandyopdhyay, "Comparison of different turbulence models in predicting the temperature separation in a Ranque-Hilsch vortex tube," International Journal of Refrigiration, no. 33, pp. 783-792, 2010.

[7] A. Secchiaroli, R. Ricci, S. Montelpare and V. D'Alessandro, "Numerical simulation of turbulent flow in a Ranque–Hilsch vortex tube," International Journal of Heat and Mass Transfer, vol. 52, p. 5496–5511, 2009.
[8] A. G. Rajagopalan and P. J. Disimile, "Geometric Modifications and Their Impact on the Performance of the Vortex Tube," International Journal on Theoretical and Applied Research in Mechanical Engineering, vol. 4, no. 3, 2015.
[9] H. Thakare R, A. Monde and A. Parekh D, "Experimental, computational and optimization studies of temperature separation and flow physics of vortex tube: A review," Renewable and Sustainable Energy Reviews, no. 52, pp. 1043-1071, 2015.
[10] A. R. Bramo and N. Pourmahmoud, "Computational Fluid Dynamics Simulation of Length to Diameter Ratio Effects on the Energy Separation in a Vortex Tube," Thermal Science, vol. 15, no. 3, pp. 833-848, 2011.
[11] H. M. Skye, G. F. Nellis and S. A. Klein, "Comparison of CFD analysis to empirical data in a commercial vortex tube," International Journal of Refrigeration, vol. 29, pp. 71-80, 2006.
[12] B. E. Launder, A. Morse, W. Rodi and D. B. Spalding, "Prediction of Free Shear Flows: A Comparison of The Performance of Six Turbulence Models," in Proceedings of conference on free turbulent shear flows - Vol. 1, 1973.
[13] M. G. D. Fokke, T. L. Liem, J. J. Derksen and H. E. A. Van Den Akker, "LDA and LIF Experiments on the quasi-periodic and complex flow in a cyclone," 1994.
[14] M. Woelke, "Eddy Viscosity Turbulence Models Employed by Computational Fluid Dynamics," Transactions of the Institute of Aviation, no. 191, pp. 92-113.
[15] S. Hogg and M. A. Leschziner, "Computation of Highly Swirling Confined Flow with a Reynolds Stress Turbulence Model," AIAA, vol. 27, no. 1, pp. 57-63, 1989.
[16] J. C. Chen and C. A. Lin, "Computations of Strongly Swirling Flows with Second-Moment Closures," International Journal for Numerical Methods in Fluids, vol. 30, p. 493–508, 1999.
[17] J. J. Derksen and H. E. A. Van Den Akker, "Simulation of Vortex Core Precession in a Reverse-Flow Cyclone," American Institute of Chemical Engineers, vol. 46, no. 7, pp. 1317-1331, July 2000.